

# Dynamic Evolution of Antisite Defect and Coupling Anionic Redox in High-Voltage Ultrahigh-Ni Cathode

Kang Wu, Peilin Ran, Wen Yin, Lunhua He, Baotian Wang, Fangwei Wang, Enyue Zhao,\* and Jinkui Zhao\*

**Abstract:** High-voltage ultrahigh-Ni cathodes ( $\text{Li-Ni}_x\text{Co}_y\text{Mn}_{1-x-y}\text{O}_2$ ,  $x \geq 0.9$ ) can significantly enhance the energy density and cost-effectiveness of Li-ion batteries beyond current levels. However, severe Li–Ni antisite defects and their undetermined dynamic evolutions during high-voltage cycling limit the further development of these ultrahigh-Ni cathodes. In this study, we quantify the dynamic evolutions of the Li–Ni antisite defect using operando neutron diffraction and reveal its coupling relationship with anionic redox, another critical challenge restricting ultrahigh-Ni cathodes. We detect a clear Ni migration coupled with an unstable oxygen lattice, which accompanies the oxidation of oxygen anions at high voltages. Based on these findings, we propose that minimized Li–Ni antisite defects and controlled Ni migrations are essential for achieving stable high-voltage cycling structures in ultrahigh-Ni cathodes. This is further demonstrated by the optimized ultrahigh-Ni cathode, where reduced dynamic evolutions of the Li–Ni antisite defect effectively inhibit the anionic redox, enhancing the 4.5 V cycling stability.

affordable costs.<sup>[1]</sup> Ni-rich layered oxides  $\text{LiNi}_x\text{M}_{1-x}\text{O}_2$  ( $\text{M}=\text{Co}, \text{Mn}, \text{Al}, \text{etc.}, x > 0.5$ ) have emerged as promising LIB cathodes due to their energy density and cost advantages.<sup>[2]</sup> Increasing the Ni content to an ultrahigh level ( $\text{Ni} \geq 0.9$ ) further enhances these advantages but exacerbates the issue of Li–Ni antisite defects (i.e., Li–Ni intermixing).<sup>[3]</sup> Over the past few decades, extensive studies have been conducted on Li–Ni antisite defects, focusing on their driving forces and tuning methods.<sup>[4]</sup> Although the optimal degree of Li–Ni intermixing within a pristine structure remains debatable, there's consensus that these defects significantly affect electrochemical performance.<sup>[5]</sup> Quantum mechanical calculations suggest that Li–Ni antisite defects are dynamic, with Ni migrations occurring upon cycling.<sup>[6]</sup> However, suitable characterization techniques to quantify these dynamic evolutions have been limited, leaving the dynamic influence of these defects on cycling structure stability an open question, hindering further structural optimizations of ultrahigh-Ni cathodes.

Additionally, most research has focused on intermixed Ni in the Li layer, neglecting intermixed Li in the transition-metal (TM) layer.<sup>[7]</sup> Intermixed Ni in the Li layer is reported to slow Li-ion diffusion and brace the structure, whereas intermixed Li in the TM layer can form a Li–O–Li configuration (Figure 1).<sup>[6a,8]</sup> The nonbonding oxygen *p*-orbital ( $\text{O}2p$ ) state along this configuration triggers anionic ( $\text{O}^{2-}$ ) redox activity (Figure 1), making anions compete with cations for charge compensation, particularly at high voltages.<sup>[9]</sup> Anionic redox, however, often leads to oxygen release, resulting in structural degradation and electrochemical failure (Figure 1).<sup>[8d,10]</sup> The formed oxygen vacancies ( $\text{V}_\text{O}$ ) can theoretically facilitate Ni migrations from the TM layer to the Li layer, exacerbating the antisite defect.<sup>[11]</sup> Notably,  $\text{V}_{\text{Ni}}\text{O-Li}$  and  $\text{V}_{\text{Ni}}\text{O-V}_{\text{Li}}$  configurations can form alongside Ni migrations and Li extractions, promoting anionic redox and destabilizing the oxygen lattice.<sup>[12]</sup> This scenario becomes more pronounced at higher charging cut-off voltages. Therefore, an in-depth understanding of the dynamic coupling process between Ni migrations and anionic redox is essential for developing high-voltage (e.g., 4.5 V) ultrahigh-Ni cathodes.

Neutron powder diffraction (NPD) is a powerful tool for analyzing the Li–Ni antisite defect. Compared to X-rays and electrons, neutrons are sensitive to light elements such as Li and O, and they can distinguish neighboring TM elements like Ni, Mn, and Co.<sup>[13]</sup> When combined with the operando method, dynamic TM migrations and coupled structure

## Introduction

The rapid electrification of the automobile industry calls for Li-ion batteries (LIBs) with both high energy density and

[\*] K. Wu, P. Ran, L. He, F. Wang, E. Zhao, J. Zhao  
 Songshan Lake Materials Laboratory, Dongguan 523808, China  
 E-mail: eyzhao@sslslab.org.cn  
 jkzhao@sslslab.org.cn

K. Wu, P. Ran, L. He, F. Wang, J. Zhao  
 Beijing National Laboratory for Condensed Matter Physics, Institute of Physics, Chinese Academy of Sciences, Beijing 100190, China

K. Wu  
 College of Chemical Engineering and Safety, Shandong university of aeronautics, Binzhou, Shandong 256600, China

W. Yin, L. He, B. Wang, F. Wang  
 Spallation Neutron Source Science Center, Dongguan 523803, Guangdong, China

W. Yin, B. Wang  
 Institute of High Energy Physics, Chinese Academy of Sciences, Beijing 100049, China

J. Zhao  
 School of Physical Sciences, Great Bay University, Dongguan 523808, China

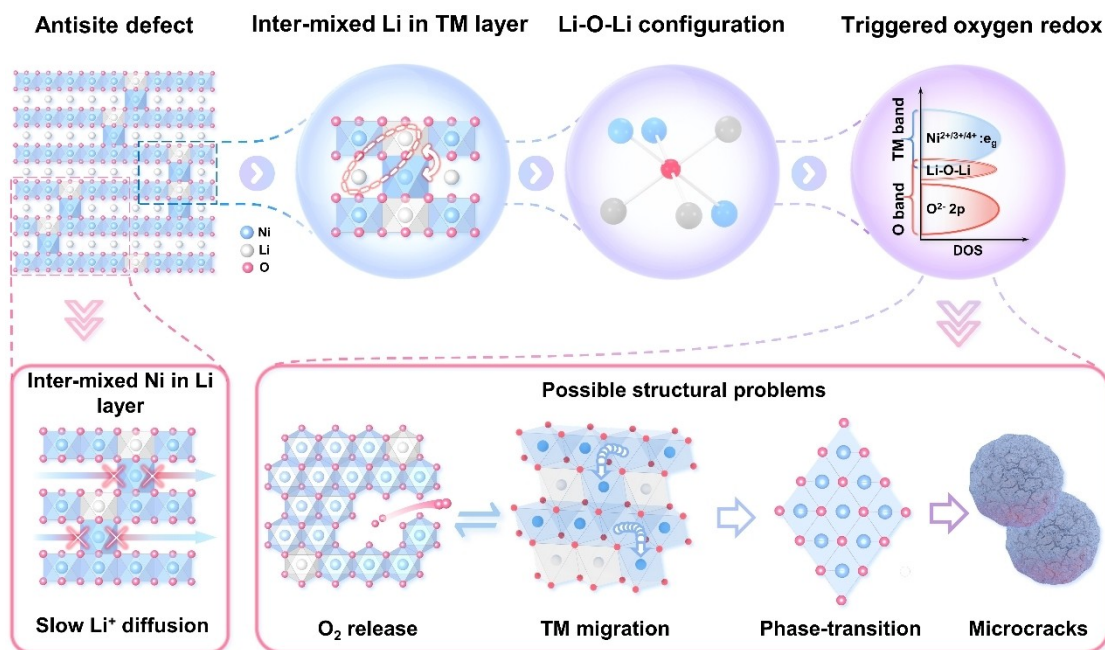


**Figure 1.** Two aspects of antisite defect's impact on the structure of ultrahigh-Ni cathodes: (1) the inter-mixed Ni in the Li layer can slow Li-ion diffusion while bracing the structure; (2) the inter-mixed Li in the TM layer can trigger high-voltage anionic redox, leading to unfavorable structure evolutions such as O<sub>2</sub> release, coupled TM migrations, irreversible phase transitions, and particle microcracks.

evolutions associated with the oxygen lattice can be precisely quantified using neutron diffraction.

To avoid the high neutron absorption of the <sup>6</sup>Li isotope, we designed the LiNi<sub>0.9</sub>Co<sub>0.05</sub>Mn<sub>0.05</sub>O<sub>2</sub> (NCM90) model compound using the <sup>7</sup>Li isotope. Through operando neutron diffraction, we discovered a sudden increase in Ni migrations at high voltages coinciding with anionic oxidation, providing direct evidence for the strong coupling between Li–Ni antisite defects and anionic redox. Next, we reduced the pristine-structure Li–Ni intermixing of NCM90 using a dual-site Mg doping strategy, which decreases Li–O–Li configurations and constructs new Li–O–Mg configurations, thereby lowering anionic redox activity.<sup>[14]</sup> The modified NCM90 showed suppressed Ni migrations, which further inhibits the anionic redox. It demonstrated superior 4.5 V cycling performance and thermal stability. This work highlights the importance of tuning dynamic Li–Ni antisite defects in developing high-voltage Ni-rich cathodes.

## Results and Discussion

### Dynamic and Coupled Structural Evolutions

To evaluate the dynamic structure evolutions upon cycling, a single-layer pouch cell with an NCM90 cathode and graphite anode was designed for operando neutron diffraction measurements (Figure 2a). As expected, samples synthesized with the <sup>7</sup>Li isotope yielded good neutron diffraction data with high signal-to-noise ratios (Figure 2b and 2c), greatly facilitating subsequent data analysis. The refinement of neutron diffraction data indicated a 2.2% Li–Ni intermix-

ing in the pristine NCM90 sample (Figure 2b and Table S1). Such inevitable Li–Ni antisite defects can lead to Li–O–Li configurations with nonbonding O2p states, triggering anionic redox reactions (ARR) in the NCM90 cathode (Figure 1). The ARR process readily causes oxygen release, weakening Ni–O coordination bonding and facilitating Ni movements. Meanwhile, the produced oxygen vacancies reduce the energy barrier for Ni migrations through the oxygen plane (Figure 2e). As revealed by the refinement results of the operando neutron diffraction patterns, during the Li de-lithiation process, there are dynamic Ni migrations from the TM layer to the Li layer, particularly at high voltages when oxidation of lattice oxygen is involved in charge compensation (Figure 2c and the left panel of Figure 2d). Notably, the increased Ni migration can induce the formation of V<sub>Ni</sub>–O–Li and V<sub>Ni</sub>–O–V<sub>Li</sub> configurations, further enhancing anionic redox reactivity at high voltages and destabilizing the oxygen lattice framework. The increased instability of the oxygen lattice is supported by the refined oxygen-atomic isotropic temperature factor (*U*<sub>iso</sub>), a parameter closely correlated with oxygen thermal motion. Generally, the higher the oxygen-atomic isotropic temperature factor, the more unstable the oxygen lattice. The middle panel of Figure 2d indicates a sudden increase in the oxygen-atomic temperature factor associated with a severe rise in Ni migrations. Additionally, increased lattice stress unfavorable for cycled structure stability is observed at high voltages (right panel of Figure 2d). The consistent variation trend of lattice stress with dynamic Ni migrations and the oxygen-atomic isotropic temperature factor indicates that the sudden increased stress is strongly associated with activated anionic redox and dynamic Ni migrations (Fig-

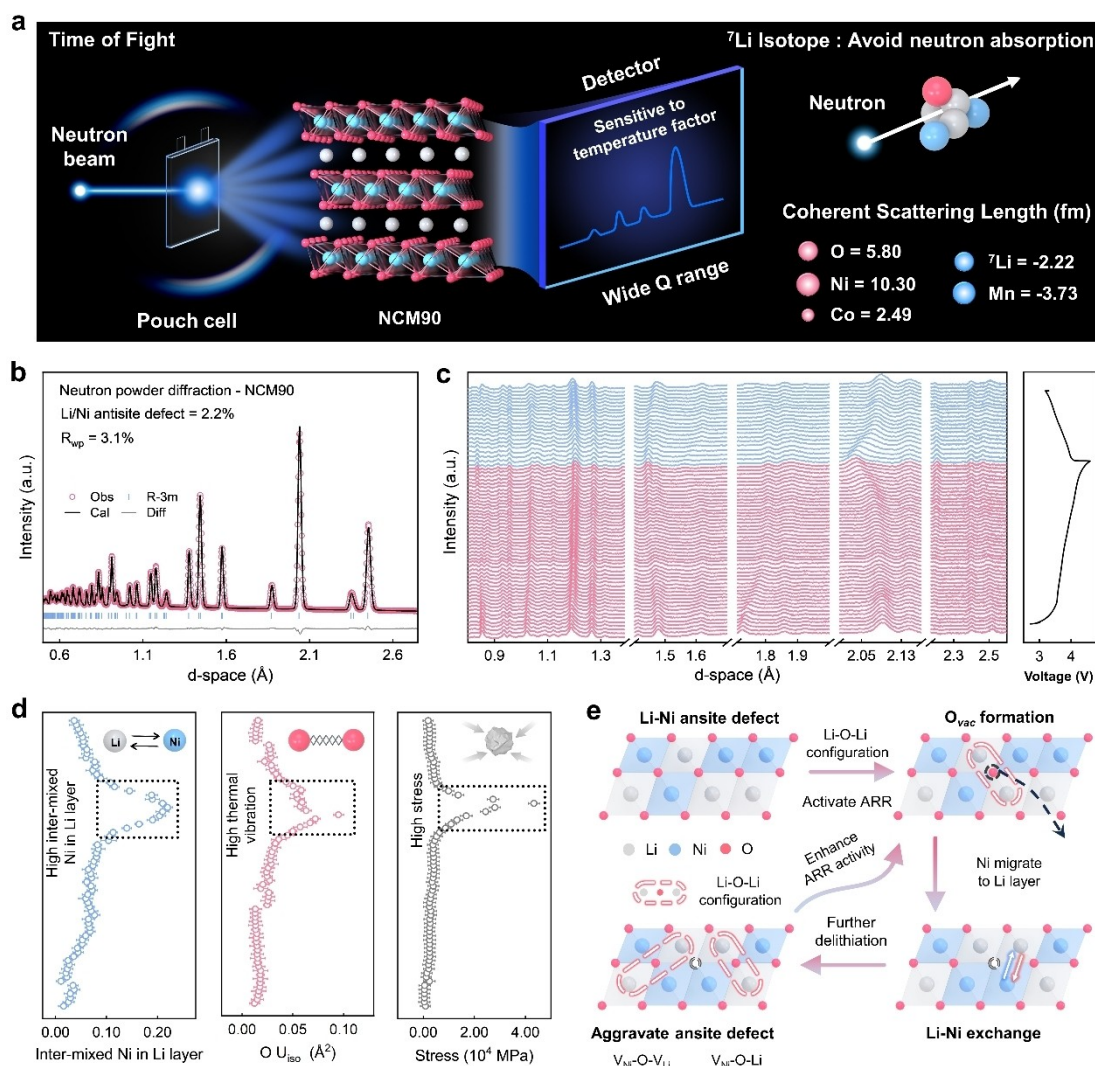


**Figure 2.** (a) Schematic of the operando neutron diffraction experiment and illustration of advantages of the neutron diffraction technique; (b) Neutron diffraction patterns and refinement results of the NCM90 powder sample; (c) Stacked neutron diffraction data collected during the operando electrochemical cycling (left panel) and the corresponding initial charge/discharge curve of the NCM90/graphite pouch cell (right panel); (d) Evolution of Ni migrations (left panel), oxygen  $U_{iso}$  (middle panel) and structural stress (right panel) upon cycling. The results are observed based on the refinements of operando neutron diffraction data; see also lattice parameter evolutions in Figure S2; (e) Schematic illustration of coupling relations among antisite defect, anionic redox, and dynamic structure evolutions. A high Li–Ni antisite defect facilitates anionic redox at high voltages, which readily causes oxygen release and further induces Ni migrations. This leads to an increase in nonbonding oxygen states ( $V_{Ni}-O-Li$  and  $V_{Ni}-O-V_{Li}$  configurations), which in turn trigger anionic redox and aggravate irreversible structural reconstructions.

ure 2d). Overall, the coupled anionic redox, Li–Ni antisite defects, and dynamic Ni migrations destabilize the cycled structure, leading to structural degradations and inferior cycle lifespan of the high-voltage NCM90 cathode.

The above analysis also leads to a reassessment of the role of Li–Ni antisite defects in ultrahigh-Ni cathodes. For low-voltage (such as 4.3 V) ultrahigh-Ni cathodes, a moderate Li–Ni antisite defect is reported to be favorable for cycled structure stability due to the pillar role of intermixed Ni in the Li layer.<sup>[3a,6a,8a,b,14c]</sup> Although the nonbonding  $O2p$  states caused by Li–Ni antisite defects can increase oxygen band energy, a high enough charging voltage is also required to activate anionic redox. Usually, for low-voltage ultrahigh-Ni cathodes, charge compensation is mainly provided by TM

cationic redox, with less participation from oxygen anionic redox. The positive effect of the Li–Ni antisite defect outweighs its negative one. For high-voltage ultrahigh-Ni cathodes, however, the scenario is reversed. Therefore, controlling Li–Ni antisite defects, particularly dynamic Ni migrations, is essential for developing high-voltage (such as 4.5 V) ultrahigh-Ni cathodes.

#### Tuning Antisite Defects and Optimizing Electrochemical Properties

To control the Li–Ni antisite defect, various elements with different electronic structures (Na, Mg, Al, Cu, Fe, Ti, Zr,

Ru, Nb, Mo, W, Ta, and Y) were introduced as dopants for synthesizing NCM90 samples (Figure 3a). Heterogeneous elements have been reported to optimize Ni-rich cathodes, but few studies focus on 4.5 V ultrahigh-Ni cathodes, and systematic studies of their effects on Li–Ni antisite defects are lacking.<sup>[15]</sup> To evaluate the dopants' role in reducing the Li–Ni antisite defect and improving electrochemical properties, we optimized the doping content for each element (Figure S3–S29). Figure 3b–3d show the results using the optimal doping levels. The degree of Li–Ni intermixing is reflected in the intensity ratio between the (003) and (104) X-ray diffraction peaks.<sup>[16]</sup> A higher ratio indicates a lower Li–Ni antisite defect. Among all the dopants, Mg demonstrates a significant advantage in reducing the intrinsic Li–Ni antisite defect (Figure 3b). As expected, the Mg dopant enables the NCM90 cathode to achieve outstanding high-voltage electrochemical performance, including the highest initial reversible capacity (234 mAh g<sup>-1</sup>) and the highest residual capacity after 100 cycles at 1 C (215 mAh g<sup>-1</sup>) (Figure 3c and 3d). The effects of other dopants on Li–Ni antisite defects and electrochemical properties are briefly discussed in the supporting materials.

To gain a deeper understanding of the Mg dopant's influence on high-voltage NCM90 cathodes, we conducted systematic electrochemical and structural measurements. The optimal molar ratio for Mg doping was determined to be 0.5% (based on TM content). Therefore, for subsequent

measurements, we selected the 0.5% Mg-doped NCM90 (denoted as 0.5Mg-NCM90) cathode as the model compound.

Due to reduced Li–Ni intermixing, the 0.5Mg-NCM90 cathode shows enhanced Li diffusion kinetics (supported by Galvanostatic Intermittent Titration Technique data in Figure S31) and improved rate capability (Figure S32). In addition to increased capacity retention, the voltage decay is also suppressed via the control of Li–Ni intermixing. After 100 cycles at 1 C, the average voltage attenuation rate of the 0.5Mg-NCM90 cathode is 0.017% (i.e., 0.407 mV per cycle), much lower than the 0.035% (i.e., 0.824 mV per cycle) of the NCM90 cathode (Figure S33). The superior 4.5 V capacity and voltage retention of the 0.5Mg-NCM90 cathode are attributed to its structural stability upon Li de/intercalation, as reflected in dQ/dV curves (Figure 4a and 4b).

During the charging process, ultrahigh-Ni cathodes usually undergo three phase transitions: the original layered structure (H1) transforms to the monoclinic phase (M), then to the second hexagonal phase (H2), and finally to the third hexagonal phase (H3). This H2–H3 transition causes detrimental lattice shrinkage along the c-direction, resulting in volume changes and local stress accumulation.<sup>[17]</sup> It has also been reported that the cycling structure stability of ultrahigh-Ni cathodes is closely associated with the reversibility of the H2–H3 transition. As indicated in Figure 4a and 4b, compared with the NCM90 cathode, the 0.5Mg-NCM90

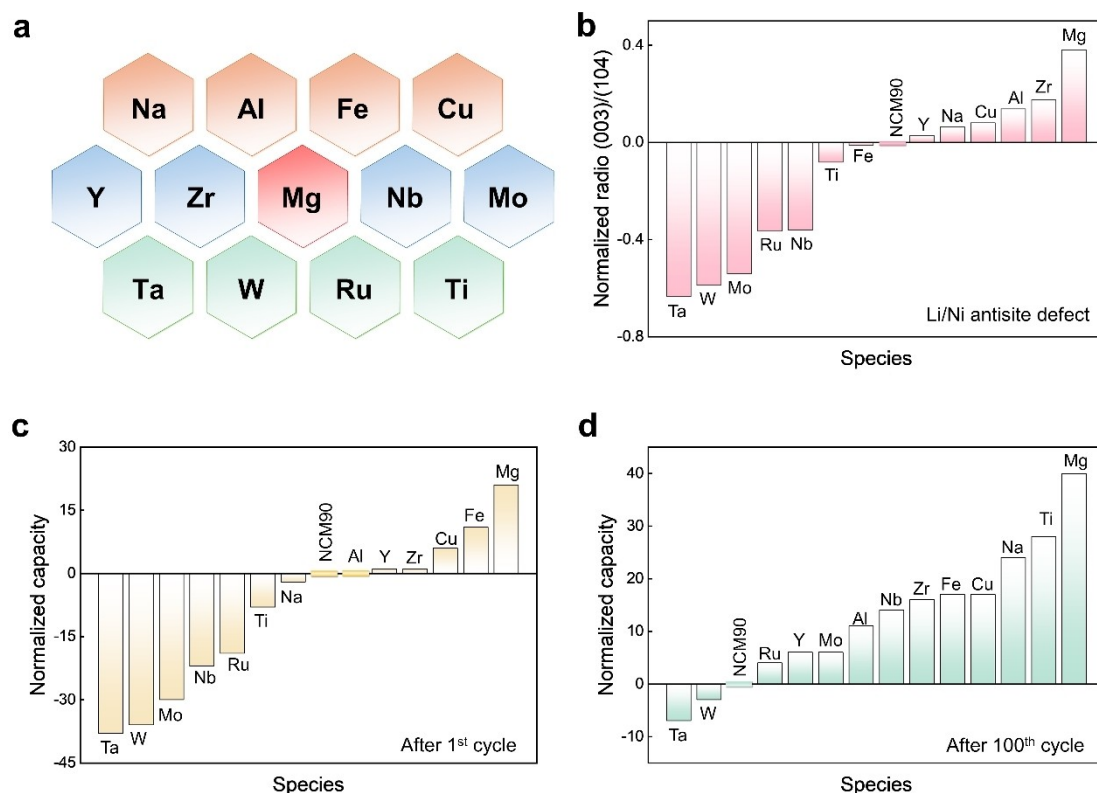


**Figure 3.** (a) Heterogeneous elements selected in this work; (b–d) Properties for these elements: (b) The normalized (003) and (104) X-ray powder diffraction (XRD) peak intensity ratios; The normalized discharge capacity at 1 C for optimal doping after (c) initial and (d) 100 cycles. The corresponding XRD patterns and more detailed electrochemical data are presented in Figure S3–S29.

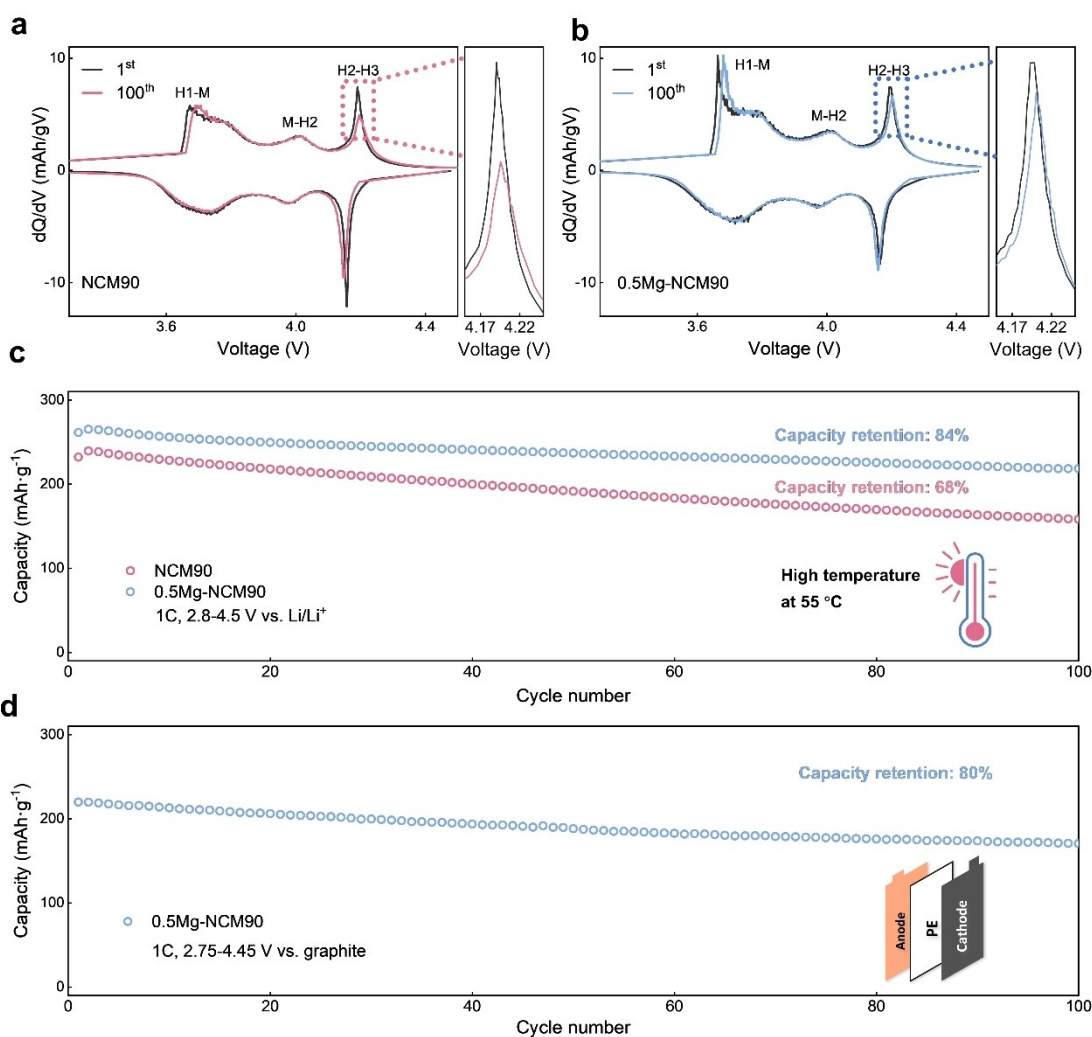


**Figure 4.** The differential capacity ( $dQ/dV$ ) vs. voltage curves upon cycling at 1 C for the (a) NCM90 and (b) 0.5Mg-NCM90 cathodes; (c) The high temperature ( $55\text{ }^{\circ}\text{C}$ ) cycle performance at 1 C for the NCM90 and 0.5Mg-NCM90 cathodes; (d) The pouch-cell cycle performance for the 0.5Mg-NCM90 cathode.

cathode shows a more reversible H2-H3 transition after 100 cycles.

The long cycle properties at  $55\text{ }^{\circ}\text{C}$  were studied to explore the role of lowered Li-Ni intermixing in the thermal stability of 0.5Mg-NCM90. The initial reversible capacities of NCM90 and 0.5Mg-NCM90 electrodes were  $232$  and  $260\text{ mAh g}^{-1}$ , respectively, and then decayed to  $158$  and  $218\text{ mAh g}^{-1}$  at 1 C after 100 cycles. These data correspond to capacity retention values of 68% and 84%, respectively, indicating that there is an optimized thermal structure stability of the 0.5Mg-NCM90 (Figure 4c, Figure S34). For further practical-application evaluation of the 0.5Mg-NCM90 cathode, a single-layer pouch cell was assembled. The charging and discharging tests for the pouch cell were performed in the voltage range of  $2.75\text{--}4.45\text{ V}$  (vs. graphite) at 1 C at room temperature. The 0.5Mg-NCM90 pouch cell shows a notable capacity retention rate of up to 80% (Figure 4d). Meanwhile, the energy density of 0.5Mg-NCM90 electrode is improved remarkably at 1 C in the voltage of  $2.8\text{--}4.5\text{ V}$  (Figure S35), and the above excellent

electrochemical properties are attributed to the reduced pristine-structure Li-Ni intermixing and maintained robust structure stability.

#### Reduced and Stabilized Oxygen Redox

We conducted high-resolution neutron powder diffraction measurements to further quantify the Li-Ni intermixing in 0.5Mg-NCM90. Diffraction data refinement results indicate a reduced Li-Ni antisite defect (only 1%) for 0.5Mg-NCM90 (Figure S36 and Table S2). Interestingly, we found that Mg ions are doped not only into the TM layer but also into the Li layer. This may be because  $\text{Mg}^{2+}$  and  $\text{Li}^{+}$  have similar ionic radii. The Mg in the Li layer can act as a pillar, stabilizing the cycled structure similarly to the intermixed Ni in the Li layer. Although introducing Mg into the TM layer can create new Li-O-Mg configurations with nonbonding  $\text{O}2p$  states, the resulting anionic redox activity is weaker than that of the Li-O-Li configurations. Thus, the high-

voltage 0.5Mg-NCM90 cathode with reduced Li–Ni antisite defect is expected to exhibit lowered ARR activity upon cycling. Density-function theory (DFT) studies further determined that introducing Mg increased the Li–Ni exchange energy (Figure S37–S39).

To demonstrate the inhibited ARR activity and stable oxygen lattice framework in 0.5Mg-NCM90, we collected ex situ O K-edge sXAS data in TFY mode which is sensitive to the bulk electronic structure (Figure 5a and 5b).<sup>[18]</sup> The pre-edge features near 532 eV are related to the transition from O1s to 2p, and their intensity is related to the density of unoccupied TM 3d-O 2p  $t_{2g}$  hybridized states. The peak at the higher energy of 545 eV represents a hybrid state of TM 3d-O 2p  $e_g$  electron orbitals. When discharged to 2.8 V, the shape of the pre-edge peak for the NCM90 cathode significantly changes due to strong ARR activity, accompanied by an unstable and irreversible ARR process of oxygen gas release.<sup>[19]</sup> For the 0.5Mg-NCM90 cathode, the ex situ pre-edge peak shows almost no change, demonstrating relatively weak ARR activity and a reversible ARR process.

The reduced and stable ARR activity in the 0.5Mg-NCM90 cathode is further demonstrated by ex situ EPR measurements (Figure 5c). During the charging process, the observed EPR peak at 3280–3360 G is associated with the oxidation of oxygen ions. The higher the peak intensity, the higher the ARR activity and the more superoxide products. Excessive superoxide can cause the release of oxygen, which is detrimental to the oxygen lattice stability.<sup>[20]</sup> As indicated in Figure 5c, compared with the NCM90 cathode, the 0.5Mg-NCM90 cathode exhibits a lower peak intensity at high-voltage charging states, suggesting the inhibited ARR activity.<sup>[21]</sup> The DFT data support the EPR results (Fig-

ure 5d). For both the 4.5 V-charged calculation models of NCM90 and 0.5Mg-NCM90, there is an obvious accumulation of O2p DOS around the Fermi level. However, compared with NCM90, the Mg-NCM90 model shows a lower O2p DOS intensity around the Fermi level, indicating decreased ARR activity.<sup>[22]</sup>

Additionally, operando DEMS measurements provide more direct evidence for the inhibited ARR activity and stable oxygen framework in 0.5Mg-NCM90. As indicated in Figure 5e and 5f, the produced O<sub>2</sub> gas in the 0.5Mg-NCM90 cathode is much lower than that of the NCM90 cathode. The above conclusions that inhibited ARR activity in 0.5Mg-NCM90 are further verified by NPD refinement data (Figure S43). The reduced O<sub>2</sub> release also suppresses surface side reactions of the 0.5Mg-NCM90 cathode, as revealed by the semi-quantitative analysis of the ex situ X-ray photoelectron spectroscopy data (Figure S44 and S45, Table S7). The cathode electrolyte interphase (CEI) has been an indicator of the degree of surface-side reactions. For example, at a 4.5 V-charged state, the CEI layer's thickness of the 0.5Mg-NCM90 cathode is 4 Å, thinner than the 8 Å value of the NCM90 cathode (Figure S46). The inorganic component LiF is an excellent electronic insulator, which can prevent electron tunneling and hinder the decomposition of the electrolyte. LiF is generally considered a favorable CEI component. The thinner CEI layer and more abundant LiF content of 0.5Mg-NCM90 indicate a more stable surface structure upon cycling.<sup>[23]</sup>

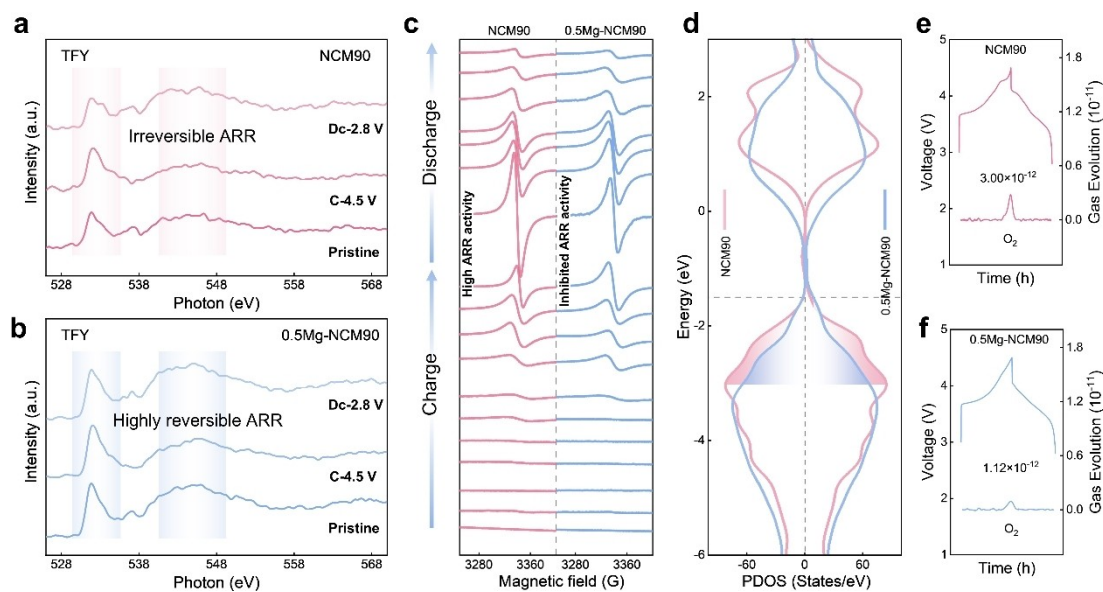


**Figure 5.** The ex situ O K-edge soft X-ray absorption spectroscopy (sXAS) data in total fluorescence yield (TFY) mode collected at pristine, C-4.5 V, and Dc-2.8 V states for the (a) NCM90 and (b) 0.5Mg-NCM90 electrodes; (c) The ex situ electron paramagnetic resonance (EPR) data collected at various states of charge and discharge during the initial cycling process of NCM90 and 0.5Mg-NCM90 electrodes; (d) The calculated projected density of states (DOS) results for the Li-extracted NCM90 and 0.5Mg-NCM90 models (corresponding to the C-4.5 V state). The operando differential electrochemical mass spectrometry (DEMS) results for the (e) NCM90 and (f) 0.5Mg-NCM90 electrodes.

### Suppressed Dynamic Ni Migration

The dynamic Ni migration in the 0.5Mg-NCM90 is also suppressed, as further confirmed by neutron diffraction data collected at the 4.5 V charged state (C-4.5 V). The refinement results show that the Li–Ni intermixing for the C-4.5 V NCM90 cathode is 20%, which is much higher than the 9% for the C-4.5 V 0.5Mg-NCM90 cathode (Figure 6a and 6b, Tables S5, S6). Compared with the pristine state, after charged to 4.5 V, there is about 18% Ni migration into the Li layer for the NCM90 cathode, while only 8% Ni migrated into the Li layer for the 0.5Mg-NCM90 cathode (Figure 6c and 6d). The suppressed dynamic Ni migration is closely associated with the low Li–Ni antisite defect and reduced ARR activity. As supported by DFT calculations (Figure 6i, Figure S49 and S50), the Ni migration energy barrier for the 4.5 V charged Mg-NCM90 model (4.68 eV) is higher than that for the NCM90 model (2.74 eV). Meanwhile, due to the severe Ni migrations in the NCM90 cathode, inevitable structure reconstructions, such as rock-salt NiO impurity phase, were observed by the high-resolution neutron diffraction measurements (Figure 6a). Additionally, there is an obvious increase in the oxygen atomic temperature factor and structure stress after charging to 4.5 V for the NCM90 cathode, while the 0.5Mg-NCM90 cathode shows no obvious change (Figure 6e and 6f, Figure S51, Table S5 and S6). The increased oxygen atomic temperature factor and stress in the NCM90 cathode is not favorable for the oxygen lattice structure stability. As revealed by the neutron diffraction data, there are more oxygen vacancies for the 4.5 V charged NCM90 cathode than for the 4.5 V charged 0.5Mg-NCM90

cathode (Figure 6g and 6h). This result is consistent with the operando DEMS measurements. The higher formation energy of oxygen vacancies (1.32 eV) based on DFT calculations once again supports the more stable oxygen lattice of the 0.5Mg-NCM90 cathode (Figure 6j). Both the suppressed Ni migration and well-preserved oxygen lattice framework enable the 0.5Mg-NCM90 cathode to show enhanced high-voltage long cycling stability. As directly uncovered by high-resolution transmission electron microscopy (HRTEM) and scanning electron microscopy (SEM) images collected after 100 cycles, obvious lattice distortions/breaks and a large area of secondary particle breakages were observed in the NCM90 sample, while a layered structure with straight fringes and relatively complete particle morphology is observed in the 0.5Mg-NCM90 sample (Figure S52 and S53).

### Minimized Li–Ni Intermixing Stabilized High-Voltage Cycling Structure

The multiple types of characterizations in this work not only highlight the role of low Li–Ni intermixing in improving the high-voltage ultrahigh-Ni cathode but also demonstrate the strong coupling relationships among Li–Ni antisite defects, dynamic Ni migrations, anionic redox, and high-voltage cyclic structure stability. Mg dual-site (TM & Li layer) doping resolves the high-voltage cycling structure instability of ultrahigh-Ni cathodes. As illustrated in Figure 7, the introduction of Mg reduces the Li–Ni antisite defects, thus decreasing the Li–O–Li configurations, which are the main

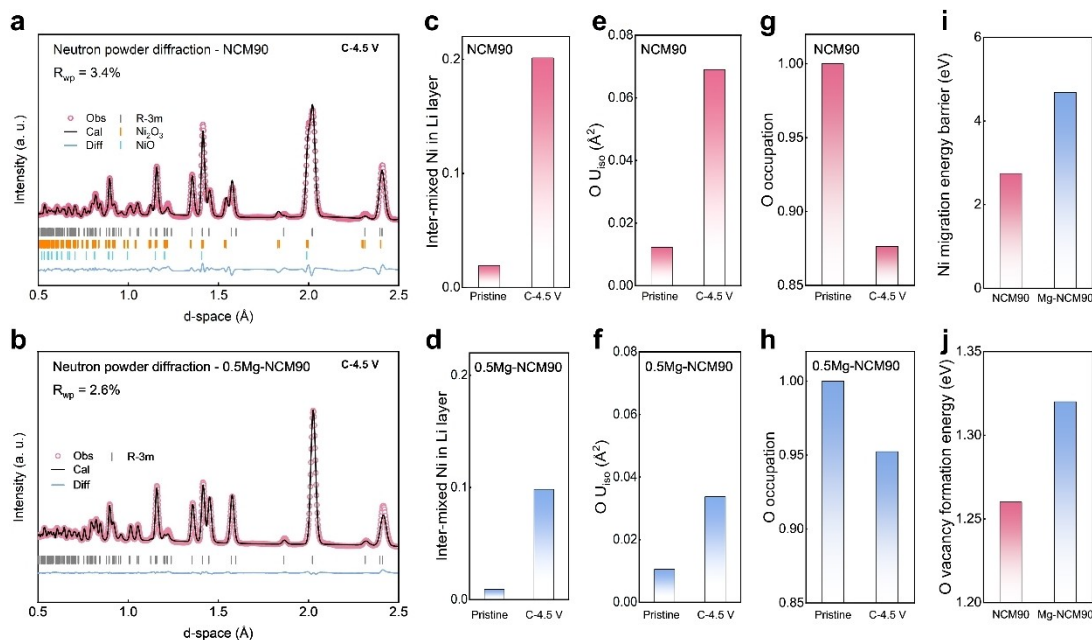


**Figure 6.** Refinement results of neutron powder diffraction data for the (a) NCM90 and (b) 0.5Mg-NCM90 electrodes collected at the C-4.5 V charge state. See also Figure S47 and S48 for the in situ XRD data of NCM90 and 0.5Mg-NCM90 electrodes collected during the initial cycling process; The inter-mixed Ni in Li layer, oxygen  $U_{iso}$  and oxygen occupation for the C-4.5 V (c,e,g) NCM90 and (d,f,h) 0.5Mg-NCM90 cathode based on the refined neutron diffraction data; (i) The DFT-calculated migration energy of Ni to Li layer and (j) DFT-calculated oxygen vacancy formation energy for the Li-extracted NCM90 and 0.5Mg-NCM90 models (corresponding to the C-4.5 V state).

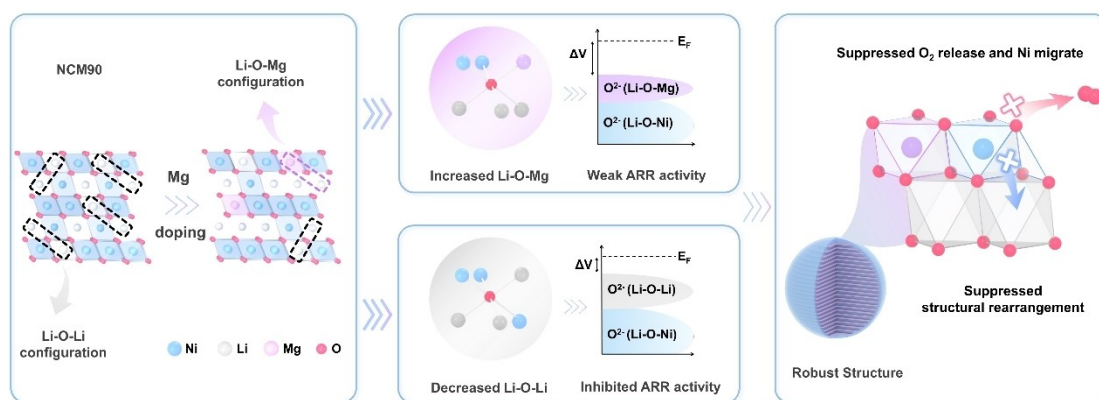


**Figure 7.** Schematic illustration of Mg doping in enhancing the cyclic structure stability: dual-site Mg doping lowers Li–Ni intermixing, inhibits anionic redox, suppresses dynamic Ni migrations, and thus leads to a robust ion-storage structure.

origin of anionic redox activity at high voltages. The Li–O–Mg configurations induced by Mg doping in the TM layer can also result in anionic redox, but their trigger requires a higher charging voltage than that of the Li–O–Li configurations. Thus, the positive role of Mg doping in the TM layer outweighs its negative role. The intrinsically reduced anionic redox activity can preserve the oxygen lattice and inhibit Ni migrations, avoiding the vicious cycle of structural instability (such as oxygen release and lattice reconstruction, Figure 2e). In addition, doping Mg into the Li layer can compensate for the absence of intermixed Ni in the Li layer, which has been reported to act as a pillar to stabilize the cyclic structure. The unique advantages of Mg doping make it an effective modification approach to stabilize high-voltage ultrahigh-Ni cathodes. Although numerous elements such as Na, Cu, Al, and Zr can also reduce Li–Ni antisite defects in NCM90 material (Figure 3b), they do not possess advantages as unique as Mg.

## Conclusion

In summary, the dynamic evolutions of the Li–Ni antisite defect in the NCM90 model compound are quantified using state-of-the-art operando neutron diffraction measurements. It is demonstrated that there is a strong coupling relationship among Li–Ni antisite defects, Ni migration, and anionic redox at high voltages. Specifically, the Li–O–Li configurations resulting from the Li–Ni antisite defect can increase anionic redox activity and promote Ni migrations. The migrated Ni can, in turn, enhance the anionic redox. Thus, reducing pristine-structure Li–Ni intermixing and inhibiting cycled-structure Ni migrations can control anionic redox and enhance high-voltage structure stability. Among the various elements with different electronic structures explored to tune the Li–Ni antisite defect and high-voltage electrochemical performance of NCM90, the Mg dual-site doping approach has been demonstrated to be most effective. Compared to 165 mAhg<sup>−1</sup> for the NCM90 with a capacity retention of 81 % after 100 cycles, a discharge capacity of 218 mAhg<sup>−1</sup> with a capacity retention of 92 % was observed

in the 0.5Mg-NCM90 cathode at 1 C. Combined with multiple in situ and ex situ characterizations, including XAS, DEMS, EPR, and NPD, as well as DFT calculations, we show that the superior 4.5 V high voltage cycling property is ascribed to inhibited anionic redox and dynamic Ni migrations enabled by lowered Li–Ni antisite defect.

## Acknowledgements

This work was supported by Guangdong Basic and Applied Basic Research Foundation (Grant No. 2022A1515010319 and 2023B1515120003), the China Postdoctoral Science Foundation (Grant No. 2022M722303), National Natural Science Foundation of China (Grant No. 12105197, 52088101 and U1932220) and Large Scientific Facility Open Subject of Songshan Lake, Dongguan, Guangdong (Grant No. KFKT2022B03). The authors thank Prof. Xiqian Yu at Institute of Physics, Chinese Academy of Sciences for the insightful discussion on the experimental results and Dr. Yuanguang Xia, Dr. Huaican Chen, Dr. Juping Xu at Spallation Neutron Source Science Center for the technique help of neutron scattering experiments.

## Conflict of Interest

The authors declare no competing financial interest.

## Data Availability Statement

The data that support the findings of this study are available from the corresponding author upon reasonable request.

**Keywords:** Li-ion Battery · Ultrahigh-Ni Cathode · Neutron Diffraction · Antisite Defect · Anionic Redox

- [1] a) L. Lu, Y. Lu, Z. Zhu, J. Shao, H. Yao, S. Wang, T. Zhang, Y. Ni, X. Wang, S. Yu, *Sci. Adv.* **2022**, *8*, 6624; b) F. Degen, M.

- Winter, D. Bendig, J. Tübke, *Nat. Energy* **2023**, 8(11), 1284–1295; c) K. Jia, J. Wang, Z. Zhuang, Z. Piao, M. Zhang, Z. Liang, G. Ji, J. Ma, H. Ji, W. Yao, *J. Am. Chem. Soc.* **2023**, 145(13), 7288–7300; d) Y. Lan, X. Li, G. Zhou, W. Yao, H. M. Cheng, Y. Tang, *Adv. Sci.* **2023**, 11(1), 2304425; e) D. Lu, R. Li, M. Rahman, P. Yu, L. Lv, S. Yang, Y. Huang, C. Sun, S. Zhang, H. Zhang, *Nature* **2024**, 627(8002), 101–107; f) L. Liang, M. Su, Z. Sun, L. Wang, L. Hou, H. Liu, Q. Zhang, C. Yuan, *Sci. Adv.* **2024**, 10, eado4472.
- [2] a) Z. Cui, A. Manthiram, *Angew. Chem. Int. Ed.* **2023**, 62(43), e202307243; b) Z. Dai, Z. Li, R. Chen, F. Wu, L. Li, *Nat. Commun.* **2023**, 14(1), 8087; c) L. Liang, X. Li, M. Su, L. Wang, J. Sun, Y. Liu, L. Hou, C. Yuan, *Angew. Chem. Int. Ed.* **2023**, 62(11), e202216155; d) Z. Qin, Z. Wen, Y. Xu, Z. Zheng, M. Bai, N. Zhang, C. Jia, H. B. Wu, G. Chen, *Small* **2022**, 18(43), 2106719; e) F. Zhao, X. Li, Y. Yan, M. Su, L. Liang, P. Nie, L. Hou, L. Chang, *J. Power Sources* **2022**, 524, 231035.
- [3] a) S. Lee, C. Li, A. Manthiram, *Adv. Energy Mater.* **2024**, 202400662; b) C. Liu, Z. Cui, A. Manthiram, *Adv. Energy Mater.* **2023**, 14(3), 202302722; c) Z. Tan, X. Chen, Y. Li, X. Xi, S. Hao, X. Li, X. Shen, Z. He, W. Zhao, Y. Yang, *Adv. Funct. Mater.* **2023**, 33(26), 202215123; d) Z. Tan, Y. Li, C. Lei, Y. Li, X. Xi, S. Jiang, F. Wu, Z. He, *Small* **2023**, 20(5), 202305618.
- [4] a) Z. Cui, X. Li, X. Bai, X. Ren, X. Ou, *Energy Storage Mater.* **2023**, 57, 14–43; b) H. Hyun, H. Yoon, S. Choi, J. Kim, S. Y. Kim, T. Regier, Z. Arthur, S. Kim, J. Lim, *Energy Environ. Sci.* **2023**, 16(9), 3968–3983; c) J. Li, W. Zhong, Q. Deng, Q. Zhang, Z. Lin, C. Yang, *Adv. Funct. Mater.* **2023**, 33(24), 202300127; d) L. Wang, R. Wang, C. Zhong, L. Lu, D. Gong, Q. Shi, Y. Fan, X. Wang, C. Zhan, G. Liu, *J. Energy Chem.* **2022**, 72, 265–275; e) Z. Wang, W. Wei, Q. Han, H. Zhu, L. Chen, Y. Hu, H. Jiang, C. Li, *ACS Nano* **2023**, 17(17), 17095–17104.
- [5] a) Y. Luo, Q. Pan, H. Wei, Y. Huang, L. Tang, Z. Wang, Z. He, C. Yan, J. Mao, K. Dai, *Nano Energy* **2022**, 102, 107626; b) T. Wang, J. Yang, H. Wang, W. Ma, M. He, Y. He, X. He, *Adv. Energy Mater.* **2023**, 13(12), 202204241; c) Z. Wu, K. Zou, X. Dai, Y.-H. Zhang, X. Zhang, H. Wang, Z. Hou, L. Ma, Y. Liu, Y. Chen, *Chem. Eng. J.* **2023**, 474, 145986.
- [6] a) Y. Song, Y. Cui, L. Geng, B. Li, L. Ge, L. Zhou, Z. Qiu, J. Nan, W. Wu, H. Xu, *Adv. Energy Mater.* **2023**, 14(7), 202303207; b) H. Wei, L. Tang, Y. Huang, Z. Wang, Y. Luo, Z. He, C. Yan, J. Mao, K. Dai, J. Zheng, *Mater. Today* **2021**, 51, 365–392; c) J. Zheng, G. Teng, C. Xin, Z. Zhuo, J. Liu, Q. Li, Z. Hu, M. Xu, S. Yan, W. Yang, *J. Phys. Chem. Lett.* **2017**, 8(22), 5537–5542.
- [7] a) H. Li, L. Wang, Y. Song, Z. Zhang, A. Du, Y. Tang, J. Wang, X. He, *Adv. Mater.* **2024**, 36(16), 202312292; b) P. Xiao, W. Li, S. Chen, G. Li, Z. Dai, M. Feng, X. Chen, W. Yang, *ACS Appl. Mater. Interfaces* **2022**, 14(28), 31851–31861; c) H. Zhang, L. Qin, M. Sedlacik, P. Saha, Q. Cheng, H. Yu, H. Jiang, *J. Mater. Chem. A* **2024**, 12(6), 3682–3688.
- [8] a) S. Jamil, C. Li, M. Fasehullah, P. Liu, F. Xiao, H. Wang, S. Bao, M. Xu, *Energy Storage Mater.* **2022**, 45, 720–729; b) J. Zhang, D. Zhou, W. Yang, J. Yang, L. Sun, G. Schumacher, X. Liu, *J. Electrochem. Soc.* **2019**, 166(16), A4097–A4105; c) S. Li, Z. Liu, L. Yang, X. Shen, Q. Liu, Z. Hu, Q. Kong, J. Ma, J. Li, H.-J. Lin, *Nano Energy* **2022**, 98, 107335; d) D. Seo, J. Lee, A. Urban, R. Malik, S. Kang, G. Ceder, *Nat. Chem.* **2016**, 8(7), 692–697.
- [9] a) X. Guo, J. Li, Y. Zhang, X. Zhang, J. Liu, W. Li, L. Lu, G. Jia, S. An, X. Qiu, *Nano Energy* **2024**, 123, 109390; b) Y. Li, S. Xu, W. Zhao, Z. Chen, Z. Chen, S. Li, J. Hu, B. Cao, J. Li, S. Zheng, *Energy Storage Mater.* **2022**, 45, 422–431; c) B. Wang, Z. Zhuo, H. Li, S. Liu, S. Zhao, X. Zhang, J. Liu, D. Xiao, W. Yang, H. Yu, *Adv. Mater.* **2023**, 35(22), 202207904.
- [10] a) X. Cao, H. Li, Y. Qiao, Z. Chang, P. Wang, C. Li, X. Yue, P. He, J. Cabana, H. Zhou, *ACS Energy Lett.* **2022**, 7(7), 2349–2356; b) E. Zhao, K. Wu, Z. Zhang, Z. Fu, H. Jiang, Y. Ke, W. Yin, K. Ikeda, T. Otomo, F. Wang, *Small Methods* **2022**, 6(11), 202200740; c) E. Zhao, M. Zhang, X. Wang, E. Hu, J. Liu, X. Yu, M. Olguin, T. A. Wynn, Y. S. Meng, K. Page, *Energy Storage Mater.* **2020**, 24, 384–393.
- [11] a) R. Komalig, G. Shukri, M. K. Agusta, M. H. Mahyuddin, A. Sumboja, A. G. Saputro, R. Maezono, A. Nuruddin, H. K. Dipojono, *Phys. Chem. Chem. Phys.* **2023**, 25(45), 31374–31381; b) J. Li, H. Yang, Q. Deng, W. Li, Q. Zhang, Z. Zhang, Y. Chu, C. Yang, *Angew. Chem. Int. Ed.* **2024**, 63(10), 202318042.
- [12] a) X. Cao, H. Li, Y. Qiao, P. He, Y. Qian, X. Yue, M. Jia, J. Cabana, H. Zhou, *Joule* **2022**, 6(6), 1290–1303; b) C. Huang, Z. Wang, H. Wang, D. Huang, Y.-B. He, S.-X. Zhao, *Mater. Today Energy* **2022**, 29, 101116.
- [13] a) J. Preimesberger, Y. Chen, K. An, C. Arnold, *J. Power Sources* **2024**, 598, 234114; b) H. Wang, D. Ning, L. Wang, H. Li, Q. Li, M. Ge, J. Zou, S. Chen, H. Shao, Y. Lai, *Small* **2022**, 18(19), 202107491; c) E. Zhao, H. Wang, W. Yin, L. He, Y. Ke, F. Wang, J. Zhao, *Appl. Phys. Lett.* **2022**, 121(11), 110501; d) E. Zhao, Z.-G. Zhang, X. Li, L. He, X. Yu, H. Li, F. Wang, *Chin. Phys. B* **2020**, 29(1), 018201.
- [14] a) H. Kim, A. Konarov, J. Jo, J. Choi, K. Ihm, H. Lee, J. Kim, S. Myung, *Adv. Energy Mater.* **2019**, 9(32), 201901181; b) U. Maitra, R. House, J. Somerville, N. Tapia-Ruiz, J. Lozano, N. Guerrini, R. Hao, K. Luo, L. Jin, M. Pérez-Osorio, *Nat. Chem.* **2018**, 10(3), 288–295; c) Y. Luo, Q. Pan, H. Wei, Y. Huang, L. Tang, Z. Wang, Y. Cheng, J. Mao, K. Dai, Q. Wu, X. Zhang, *Mater. Today* **2023**, 69, 54–65.
- [15] a) H. Ding, M. Fang, Y. Li, L. Huang, C. Zhang, X. Luo, *J. Alloys Compd.* **2023**, 946, 169428; b) L. Qiao, Q. You, X. Wu, H. Min, X. Liu, H. Yang, *ACS Appl. Mater. Interfaces* **2024**, 16(4), 4772–4783; c) Z. Tan, Y. Li, X. Xi, S. Jiang, X. Li, X. Shen, S. Hao, J. Zheng, Z. He, *ACS Sustainable Chem. Eng.* **2022**, 10(11), 3532–3545; d) T. Wang, C. Yi, P. Ge, L. Wang, W. Sun, M. Wu, C. Zhang, Y. Yang, *Sci. China Mater.* **2023**, 66(9), 3433–3444; e) T. Wang, M. Yuan, S. Xie, J. Liu, J. Yan, Z. Li, J. Peng, *Ceram. Int.* **2022**, 48(14), 20605–20611.
- [16] a) J. Morales, C. Pérez-Vicente, J. L. Tirado, *Mater. Res. Bull.* **1990**, 25(5), 623–630; b) J. Zhao, W. Zhang, A. Huq, S. T. Misture, B. Zhang, S. Guo, L. Wu, Y. Zhu, Z. Chen, K. Amine, *Adv. Energy Mater.* **2016**, 7(3), 201601266.
- [17] H. Ryu, B. Namkoong, J. Kim, I. Belharouak, C. Yoon, Y. Sun, *ACS Energy Lett.* **2021**, 6(8), 2726–2734.
- [18] Z. Zhu, D. Yu, Y. Yang, C. Su, Y. Huang, Y. Dong, I. Waluyo, B. Wang, A. Hunt, X. Yao, J. Lee, W. Xue, J. Li, *Nat. Energy* **2019**, 4, 1049–1058.
- [19] J. Song, B. Li, Y. Chen, Y. Zuo, F. Ning, H. Shang, G. Feng, N. Liu, C. Shen, X. Ai, *Adv. Mater.* **2020**, 32(16), 202000190.
- [20] B. Hu, F. Geng, M. Shen, B. Hu, *Magn. Reson. Lett.* **2023**, 3(1), 61–66.
- [21] T. Wang, Y. Zhang, W. Kong, L. Qiao, B. Peng, Z. Shen, Q. Han, H. Chen, Z. Yuan, R. Zheng, X. Yang, *Science* **2022**, 377, 1227–1232.
- [22] a) M. Freire, N. V. Kosova, C. Jordy, D. Chateigner, O. I. Lebedev, A. Maignan, V. Pralong, *Nat. Mater.* **2015**, 15(2), 173–177; b) Y. Lee, H. Park, M. Cho, J. Ahn, W. Ko, J. Kang, Y. J. Choi, H. Kim, I. Park, W. H. Ryu, *Adv. Funct. Mater.* **2022**, 32(36), 202204354.
- [23] Q. Liu, Y. Sun, S. Wang, Q. An, L. Duan, G. Zhao, C. Wang, K. Doyle-Davis, H. Guo, X. Sun, *Mater. Today* **2023**, 64, 21–30.

Manuscript received: May 31, 2024

Accepted manuscript online: July 25, 2024

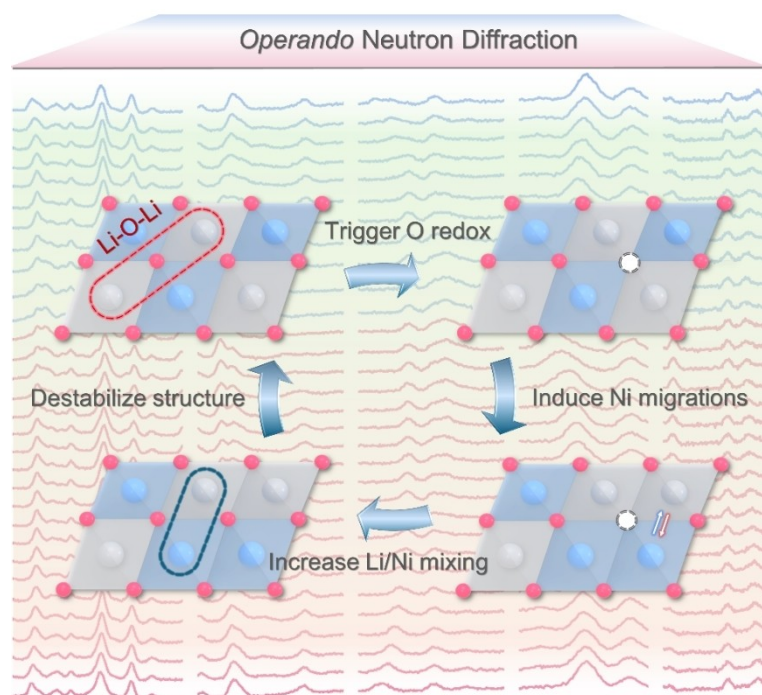
Version of record online: ■■■, ■■■

## Research Article

## Batteries

K. Wu, P. Ran, W. Yin, L. He, B. Wang,  
F. Wang, E. Zhao,\* J. Zhao\* - e202410326

Dynamic Evolution of Antisite Defect and  
Coupling Anionic Redox in High-Voltage  
Ultrahigh-Ni Cathode



The dynamic evolution of Li–Ni antisite defect and its coupling relationship with anionic redox in ultrahigh-Ni cathodes are revealed using operando neutron diffraction techniques. Further, a strategy

that minimized Li–Ni antisite defects and controlled Ni migrations for achieving stable high-voltage ultrahigh-Ni cathodes is proposed.